Stabilization of F-actin by tropomyosin isoforms regulates the morphology and mechanical behavior of red blood cells

Zhenhua Sui[a], David S. Gokhin[a], Roberta B. Nowak[a], Xinhua Guo[b], Xiuli An[b,c], and Velia M. Fowler[a,*]

[a]Department of Molecular Medicine, The Scripps Research Institute, La Jolla, CA 92037; [b]Laboratory of Membrane Biology, New York Blood Center, New York, NY 10065; [c]School of Life Science, Zhengzhou University, Henan, Zhengzhou 450001, China

ABSTRACT **The short F-actins in the red blood cell (RBC) membrane skeleton are coated along their lengths by an equimolar combination of two tropomyosin isoforms, Tpm1.9 and Tpm3.1. We hypothesized that tropomyosin's ability to stabilize F-actin regulates RBC morphology and mechanical properties. To test this, we examined mice with a targeted deletion in alternatively spliced exon 9d of *Tpm3* (*Tpm3/9d*$^{-/-}$), which leads to absence of Tpm3.1 in RBCs along with a compensatory increase in Tpm1.9 of sufficient magnitude to maintain normal total tropomyosin content. The isoform switch from Tpm1.9/Tpm3.1 to exclusively Tpm1.9 does not affect membrane skeleton composition but causes RBC F-actins to become hyperstable, based on decreased vulnerability to latrunculin-A–induced depolymerization. Unexpectedly, this isoform switch also leads to decreased association of Band 3 and glycophorin A with the membrane skeleton, suggesting that tropomyosin isoforms regulate the strength of F-actin-to-membrane linkages. *Tpm3/9d*$^{-/-}$ mice display a mild compensated anemia, in which RBCs have spherocytic morphology with increased osmotic fragility, reduced membrane deformability, and increased membrane stability. We conclude that RBC tropomyosin isoforms directly influence RBC physiology by regulating 1) the stability of the short F-actins in the membrane skeleton and 2) the strength of linkages between the membrane skeleton and transmembrane glycoproteins.**

Monitoring Editor
Thomas D. Pollard
Yale University

Received: Oct 11, 2016
Revised: Jul 14, 2017
Accepted: Jul 14, 2017

This article was published online ahead of print in MBoC in Press (http://www.molbiolcell.org/cgi/doi/10.1091/mbc.E16-10-0699) on July 18, 2017.

The authors declare no competing or financial interests.

V.M.F. and X.A. conceptualized the experiments and supervised the study. Z.S., D.S.G., R.B.N., and X.G. performed the experiments, analyzed the data, and prepared the figures. D.S.G. and V.M.F. wrote the manuscript with input from the other authors.

*Address correspondence to: Velia M. Fowler (velia@scripps.edu).

Abbreviations used: BM, bone marrow; BSA, bovine serum albumin; CytoD, cytochalasin-D; DI, deformability index; DMSO, dimethyl sulfoxide; F-actin, filamentous actin; G-actin, globular actin; GAPDH, glyceraldehyde 3-phosphate dehydrogenase; GPA, glycophorin A; GPC, glycophorin C; H&E, hematoxylin and eosin; HRP, horseradish peroxidase; LatA, latrunculin-A; MCV, mean corpuscular volume; PBS, phosphate-buffered saline; PFA, paraformaldehyde; RBC, red blood cell; RDW, red cell distribution width; TIRF, total internal reflection fluorescence microscopy; Tmod, tropomodulin; Tpm, tropomyosin.

INTRODUCTION

Beneath the plasma membranes of metazoan cells, spectrin tetramers (~200 μm long), short F-actins (~37 μm long), and associated proteins comprise a highly cross-linked, planar cytoskeletal network termed the membrane skeleton (Bennett and Baines, 2001; Bennett and Lorenzo, 2013). The membrane skeleton is tethered to the plasma membrane via interactions with adhesion receptors, transmembrane channels, and ion pumps, which exploit the membrane skeleton's long-range connectivity to establish organized membrane microdomains (Bennett and Healy, 2008; Bennett and Lorenzo, 2013). The paradigmatic membrane skeleton is the red blood cell (RBC) membrane skeleton, which, due to RBCs' lack of intracellular organelles and transcellular cytoskeleton, is an appealing model system for probing membrane skeleton architecture and function (Fowler, 2013). Disruptions of RBC membrane skeleton components due to targeted gene deletions in mice or inherited mutations in humans lead to alterations in membrane skeleton architecture, RBC morphology, and

RBC mechanical behavior, resulting in congenital hemolytic anemias of varying severities (Mohandas and Evans, 1994; Mohandas and Gallagher, 2008; Da Costa *et al.*, 2013; Fowler, 2013; Lux, 2016).

The short F-actins in the RBC membrane skeleton act as structural nodes, binding five to seven $(\alpha_1\beta_1)_2$-spectrin tetramers and serving as the vertices of the quasihexagonal membrane skeleton lattice (Fowler, 2013; Gokhin and Fowler, 2016). In addition to their structural role in lattice integrity, the F-actin nodes also tether the membrane skeleton lattice directly to the membrane via the F-actin-binding proteins, αβ-adducin and protein 4.1R, which bind to Band 3, the major integral membrane glycoprotein of RBCs (Pasternack *et al.*, 1985; Anong *et al.*, 2009). RBC F-actins are also capped at their fast-growing (barbed) and slow-growing (pointed) ends by αβ-adducin and tropomodulin1 (Tmod1), respectively, which reduce rates of subunit association/dissociation from filament ends (Fowler, 2013; Gokhin and Fowler, 2016). However, despite the F-actin-stabilizing effects of Tmod1 and αβ-adducin, RBC F-actins still exhibit important dynamic characteristics. The cytosol of intact human RBCs contains ~0.36 μM G-actin (Pinder and Gratzer, 1983; Gokhin *et al.*, 2015a), markedly greater than the barbed-end critical concentration of ~0.1 μM G-actin and, thus, sufficient for barbed-end assembly (Pollard *et al.*, 2000). RBC F-actin assembly can also be directly visualized by fluorescence microscopy of RBC ghosts resealed in the presence of rhodamine-actin and can be blocked by treatment with the barbed-end assembly inhibitor cytochalasin-D (CytoD), confirming that barbed-end assembly mediates subunit exchange in the RBC membrane skeleton (Gokhin *et al.*, 2015a). Moreover, RBC F-actin assembly and membrane mechanical properties can be selectively perturbed with the F-actin-destabilizing drug, latrunculin-A (LatA), which shifts the F:G-actin ratio towards G-actin and increases the G-actin concentration approximately twofold (Gokhin *et al.*, 2015a). Conversely, treatment of RBCs with the F-actin-stabilizing drug jasplakinolide shifts the F:G-actin ratio towards F-actin and reduces the G-actin concentration (Gokhin *et al.*, 2015a). Perturbation of the F:G-actin ratio leads to altered membrane deformability in microfluidic assays, indicating a role for actin dynamics in RBC mechanical function. However, the roles of F-actin-binding proteins in regulating the dynamic characteristics of RBC F-actins in the membrane skeleton remain unclear.

In addition to being capped by Tmod1 and αβ-adducin, RBC F-actins are also stabilized along their lengths by an equimolar ratio of two tropomyosin isoforms, Tpm1.9 (formerly TM5b) and Tpm3.1 (formerly TM5NM1) (Fowler and Bennett, 1984; Fowler, 2013; Sung and Lin, 1994; Sung *et al.*, 2000; Geeves *et al.*, 2015). Tropomyosins protect F-actin from pointed-end depolymerization in vitro (Broschat *et al.*, 1989; Broschat, 1990; Weber *et al.*, 1994) and render F-actin more mechanically rigid (Fujime and Ishiwata, 1971; Kojima *et al.*, 1994; Grazi *et al.*, 2004). The N-termini of tropomyosins also interact with Tmod1, enhancing Tmod1's ability to inhibit pointed-end depolymerization (Fowler, 1987, 1990; Weber *et al.*, 1994; Greenfield *et al.*, 2005; Kostyukova *et al.*, 2006; Kostyukova *et al.*, 2007, 2008; Lewis *et al.*, 2014; Rao *et al.*, 2014; Yamashiro *et al.*, 2014). Tropomyosins have diverse cellular functions, including promoting F-actin cable assembly and/or stability in yeast (Liu and Bretscher, 1989), contractile ring assembly during cytokinesis (Skau *et al.*, 2009; Stark *et al.*, 2010), and stress fiber formation in cultured cells (Tojkander *et al.*, 2011; for a review, see Gunning *et al.*, 2015). In RBCs, each rodlike tropomyosin molecule extends along an F-actin, possibly serving as a "molecular ruler" that dictates RBC F-actins' precise length of ~37 nm (Shen *et al.*, 1986; Fowler, 1996, 2013). RBC tropomyosins are important for RBC membrane mechanics, based on ektacytometry experiments demonstrating that Mg^{2+}-free (tropomyosin-extracted) RBC ghosts exhibit more rapid time-dependent decay in deformability (i.e., loss of mechanical stability) compared with Mg^{2+} (tropomyosin-containing) ghosts when subjected to increasing fluid shear stress (An *et al.*, 2007). RBC membrane mechanics are sensitive to tropomyosin isoform composition, as the abnormal mechanical properties of Mg^{2+}-free ghosts are rescued by reconstitution with the RBC tropomyosins Tpm1.9 and Tpm3.1 but not with skeletal muscle tropomyosins (An *et al.*, 2007).

To probe the mechanisms by which RBC tropomyosin isoforms regulate membrane skeleton architecture, F-actin dynamics, and RBC morphology and mechanical properties, we examined mice with a deletion in alternatively spliced exon 9d of *Tpm3* (*Tpm3/9d*$^{-/-}$), which lack Tpm3.1 and Tpm3.2 in all tissues (Fath *et al.*, 2010; Hook *et al.*, 2011; Lees *et al.*, 2013). (Note that only Tpm3.1 is deleted from *Tpm3/9d*$^{-/-}$ mouse RBCs, as wild-type RBCs lack Tpm3.2.) *Tpm3/9d*$^{-/-}$ mice are viable and fertile but exhibit abnormalities in in vitro neuritogenesis and in vivo skin wound healing due to disrupted F-actin in elongating neurons and migrating fibroblasts (Fath *et al.*, 2010; Lees *et al.*, 2013). Here we report that absence of Tpm3.1 in RBCs leads to a compensatory increase in Tpm1.9 in the membrane skeleton. The switch from Tpm1.9/Tpm3.1 to exclusively Tpm1.9 causes RBC F-actins to become abnormally resistant to LatA-induced depolymerization (i.e., hyperstable), demonstrating tropomyosin isoform-specific stabilization of RBC F-actins. In addition, the switch from Tpm1.9/Tpm3.1 to exclusively Tpm1.9 causes an unexpected reduction in the association of Band 3 and glycophorin A (GPA) with the Triton X-100–insoluble membrane skeleton, indicating that RBC tropomyosin isoforms differentially regulate the strength of linkages between the membrane skeleton and transmembrane glycoproteins. RBCs containing exclusively Tpm1.9 have abnormally variable spherocytic morphology, increased osmotic fragility, reduced membrane deformability, and increased membrane stability. These defects are associated with splenomegaly, increased numbers of splenic erythroblasts and circulating reticulocytes, but normal numbers of circulating RBCs—features consistent with a stress erythropoiesis response leading to a fully compensated anemia. Collectively these findings demonstrate that RBC tropomyosins influence RBC physiology via two distinct mechanisms: 1) regulation of F-actin stability in the membrane skeleton and 2) regulation of linkages between the membrane skeleton and transmembrane glycoproteins.

RESULTS

Absence of Tpm3.1 induces a compensatory increase in Tpm1.9 in RBCs, leading to reduced associations of transmembrane glycoproteins with the membrane skeleton

Tpm1.9 and Tpm3.1 are the sole tropomyosin isoforms in RBCs, present in an equimolar ratio (Fowler and Bennett, 1984; Sung and Lin, 1994; Sung *et al.*, 2000; Fowler, 2013). Western blotting of RBC ghosts confirmed that Tpm1.9 and Tpm3.1 are both present in wild-type mouse RBCs (Figure 1A), while Tpm4.2 and long muscle-type tropomyosins are absent (data not shown). Both Tpm1.9 and Tpm3.1 have punctate localization on the membranes of wild-type RBCs, based on immunostaining and total internal reflection fluorescence (TIRF) microscopy to selectively visualize the membrane interface (Mattheyses *et al.*, 2010), although Tpm3.1 localization has a pronounced diffuse component as well (Figure 1C). Western blotting confirmed that Tpm3.1 is absent from RBC ghosts prepared from *Tpm3/9d*$^{-/-}$ mouse blood (Figure 1A), as expected (Fath *et al.*, 2010; Hook *et al.*, 2011; Lees *et al.*, 2013). However, we were surprised to find that Tpm1.9 levels are increased more than twofold in Tpm3.1-null ghosts (Figure 1B)—a compensatory increase of

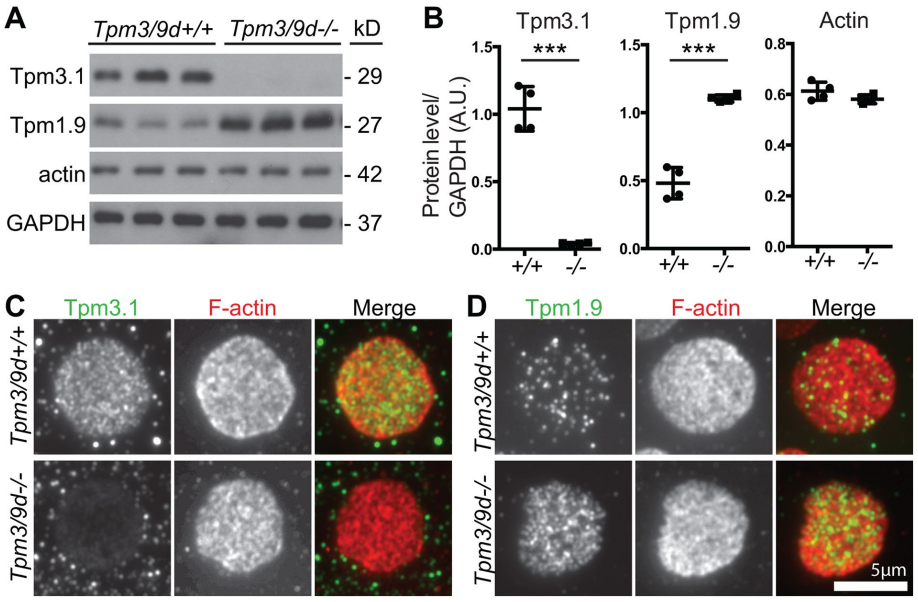

FIGURE 1: Tpm3.1-null RBCs show increased levels of Tpm1.9 associated with their membranes. (A) Western blots of Tpm3.1, Tpm1.9, actin, and GAPDH in Mg^{2+} ghosts from *Tpm3/9d*$^{+/+}$ and *Tpm3/9d*$^{-/-}$ mice. GAPDH was used as a loading control. Each lane contains ghosts from a different mouse. (B) Protein levels normalized to GAPDH determined by densitometry of the blots in A. ***, $p < 0.001$. (C, D) TIRF images of RBCs from *Tpm3/9d*$^{+/+}$ and *Tpm3/9d*$^{-/-}$ mice immunostained for (C) Tpm3.1 or (D) Tpm1.9 and phalloidin-stained for F-actin. Scale bar, 5 µm.

sufficient magnitude to restore the total tropomyosin content of Tpm3.1-null ghosts back to wild-type levels (Fowler, 2013). Consistent with this, no Tpm3.1 puncta and a marked increase in Tpm1.9 puncta were observed in Tpm3.1-null RBCs (Figure 1D).

Coomassie staining and Western blotting of Tpm3.1-null ghosts further revealed that levels of major RBC membrane skeleton proteins, including $(\alpha_1\beta_1)_2$-spectrin, Band 4.1R, Band 4.2, actin, dematin, Tmod1, and α-adducin, are unchanged (Figure 2). The levels of the major integral membrane proteins, Band 3 and GPA, are also unchanged in Tpm3.1-null ghosts, while glycophorin C (GPC) levels are increased ~40% (Figure 2). To investigate whether Tpm3.1-null RBCs had altered membrane skeleton composition and/or associations with transmembrane glycoproteins, we performed Western blotting of Triton X-100–insoluble membrane skeletons prepared from wild-type and Tpm3.1-null ghosts. This revealed a small decrease in actin in the Triton X-100–insoluble membrane skeleton, and a larger, nearly twofold, decrease in the levels of Band 3 and GPA but not GPC (Figure 2). Collectively these results show that an isoform switch from equimolar Tpm1.9/Tpm3.1 in wild-type RBCs to exclusively Tpm1.9 in Tpm3.1-null RBCs does not significantly affect the protein composition of the membrane skeleton but leads to weakened associations of Band 3 and GPA, but not GPC, with the membrane skeleton.

Tpm3.1-null ghosts containing exclusively Tpm1.9 have hyperstable F-actin

Tpm1.9 binds F-actin more strongly than Tpm3.1 in vitro (K_d of 1.84 vs. 1.05 µM, respectively; Yamashiro *et al.*, 2014), leading us to hypothesize that the switch from equimolar Tpm1.9/Tpm3.1 in wild-type RBCs to exclusively Tpm1.9 in Tpm3.1-null RBCs would increase F-actin stability in vivo. To test this, we used Western blotting to quantify cytosolic G-actin levels in intact RBCs subjected to LatA treatment (Gokhin *et al.*, 2015a). LatA treatment induces an ~3.5-fold increase in cytosolic G-actin in wild-type RBCs, and this effect is reduced by ~50% in Tpm3.1-null RBCs with increased Tpm1.9 (Figure 3), demonstrating that F-actin is abnormally stable in Tpm3.1-null RBCs. For comparison, we repeated these experiments using intact RBCs from *Tmod1*$^{-/-}$ mice, which lack Tmod1 in the membrane skeleton but show appearance of the ubiquitous Tmod3 isoform at ~20% of wild-type Tmod1 levels, leading to more variable F-actin lengths (Moyer *et al.*, 2010). Unlike Tpm3.1-null RBCs, Tmod1-null RBCs show a response to LatA treatment indistinguishable from wild-type RBCs (Figure 3), consistent with Tmod1 and Tmod3 having identical pointed-end capping activities with both of the RBC tropomyosins Tpm1.9 and Tpm3.1 (Yamashiro *et al.*, 2014). Thus tropomyosin and Tmod isoforms have distinct roles in regulating RBC F-actin stability.

Absence of Tpm3.1 in RBCs induces a stress erythropoiesis response with a fully compensated anemia

Mutant RBCs with a defective spectrin-F-actin lattice, or defective attachments to the membrane, typically have abnormal shapes and mechanical properties, resulting in compensated hemolytic anemias (Mohandas and Gallagher, 2008; Gallagher, 2013). To determine whether the switch from equimolar Tpm1.9/Tpm3.1 in wild-type RBCs to exclusively Tpm1.9 in Tpm3.1-null RBCs might affect RBC homeostasis in vivo, we performed hematological analyses. *Tpm3/9d*$^{-/-}$ mouse blood exhibits normal hemoglobin levels and hematocrit, with normal RBC, leukocyte, and platelet counts, but circulating reticulocytes are significantly elevated (Table 1), indicative of increased RBC biogenesis. In addition, *Tpm3/9d*$^{-/-}$ mouse blood shows an elevated RBC distribution width (RDW) indicative of cell size heterogeneity, as described below, and an elevated hemoglobin content per cell (total and concentration; Table 1), similar to findings in human hemolytic anemia patients with hereditary spherocytosis (Cynober *et al.*, 1996; Michaels *et al.*, 1997).

To investigate whether elevated reticulocytes in *Tpm3/9d*$^{-/-}$ mouse blood are due to stress erythropoiesis, we examined *Tpm3/9d*$^{-/-}$ bone marrow and spleen, key sites of murine steady-state and stress erythropoiesis, respectively (Paulson *et al.*, 2011). *Tpm3/9d*$^{-/-}$ mice exhibit overt splenomegaly, with a trend toward increased spleen weight that did not achieve statistical significance (Figure 4A). Histological examination of *Tpm3/9d*$^{-/-}$ spleen revealed increased red pulp by hematoxylin and eosin (H&E) staining, with normal hemoglobin distribution in the red pulp by Gömöri iron staining (Figure 4B), consistent with a murine stress erythropoiesis response. To investigate whether erythropoiesis is normal in the *Tpm3/9d*$^{-/-}$ spleen, we analyzed erythroblast terminal differentiation, a multistage process during which levels of RBC-specific cell-surface markers such as GPA increase as differentiation proceeds; simultaneously, molecules absent from circulating RBCs, such as the adhesion molecules CD44 and integrin-β_1, decrease (Chen *et al.*, 2009). Flow cytometry using Ter119 (monoclonal anti-mouse GPA; Kina *et al.*, 2000) and anti-CD44 (Chen *et al.*, 2009) identified an increased percentage of Ter119^{high} cells (mid- to late-stage erythroblasts) in

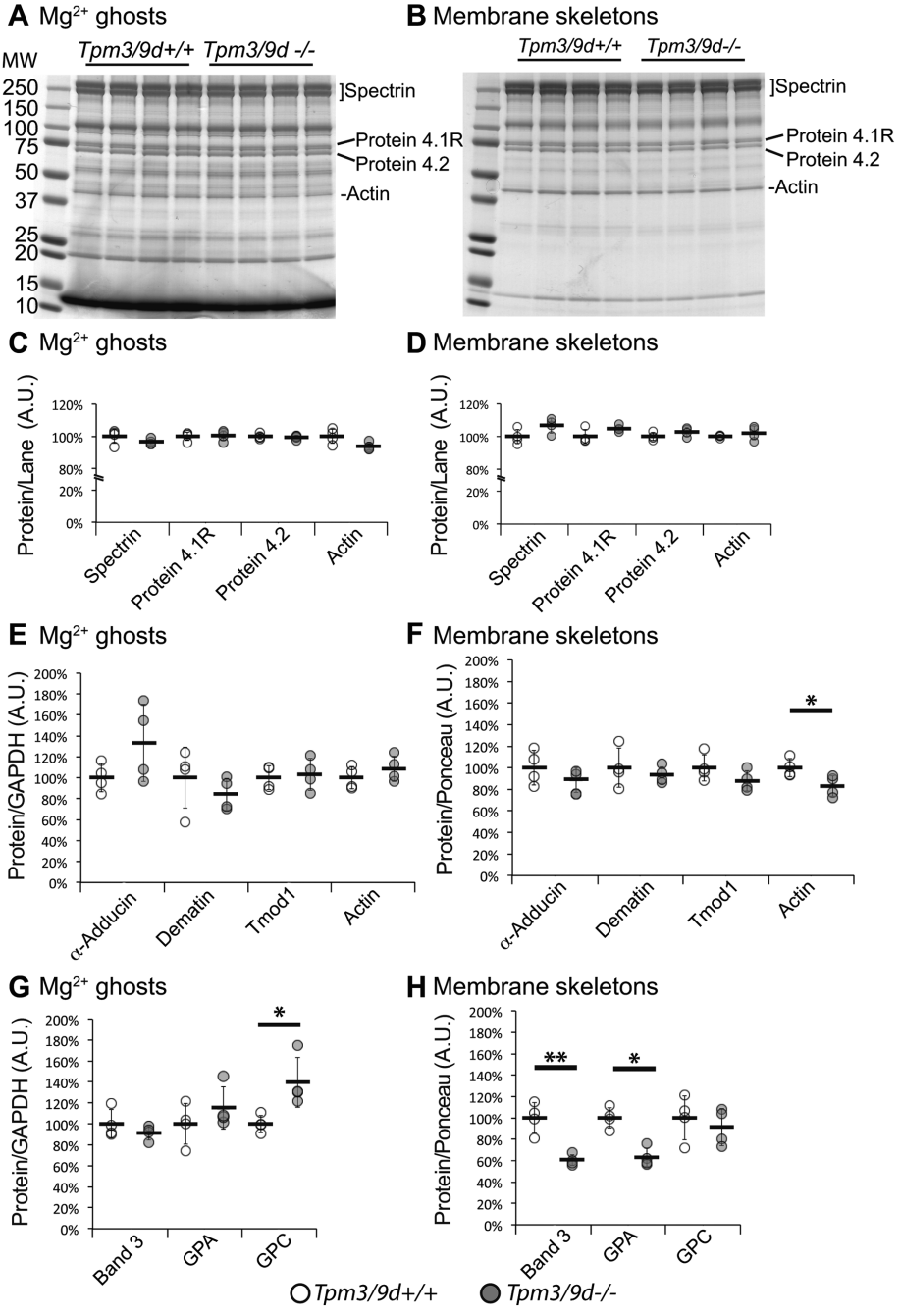

FIGURE 2: Comparison of F-actin binding proteins and major transmembrane glycoproteins in Mg^{2+} ghosts and Triton X-100–insoluble membrane skeletons prepared from *Tpm3/9d*$^{+/+}$ and *Tpm3/9d*$^{-/-}$ mice. (A, B) Coomassie blue–stained gels of (A) Mg^{2+} ghosts and (B) membrane skeletons. Each lane contains equivalent ghost volumes from a different mouse with the indicated genotypes ($N = 4$/genotype). (C, D) Quantification of $(\alpha_1\beta_1)_2$-spectrin, protein 4.1R, protein 4.2, and actin levels in (C) Mg^{2+} ghosts and (D) membrane skeletons, determined by densitometry of gels in A and B, respectively, and normalized to total Coomassie-stained protein. (E, F) Quantification of α-adducin, dematin, Tmod1, and actin levels in (E) Mg^{2+} ghosts and (F) membrane skeletons from Western blots shown in Supplemental Figure S1. (G, H) Quantification of Band 3, GPA, and GPC levels in (G) Mg^{2+} ghosts and (H) membrane skeletons from Western blots shown in Supplemental Figure S1. Protein levels on Western blots were determined by densitometry and normalized to GAPDH for ghosts (E, G) or to total protein (Ponceau S) for membrane skeletons (F, H).

Tpm3/9d$^{-/-}$ spleen (Figure 4, C and D), typical of increased erythropoiesis in the spleen, the site of stress erythropoiesis in mice (Paulson *et al.*, 2011). However, no changes in percentages of Ter119^{high} cells were observed in *Tpm3/9d*$^{-/-}$ bone marrow (Figure 4E), indicating no increase in erythropoiesis in bone marrow. In both *Tpm3/9d*$^{-/-}$ spleen and bone marrow, the distribution of Ter119^{high} erythroblast subpopulations (II–V) was unchanged, indicating no effects on progression of erythroblast terminal differentiation in absence of Tpm3.1 (Figure 4, F and G).

Next the percentage of enucleation in the P1 subpopulation of small cells identified by forward light scatter (Figure 4H, left) was examined using DNA stains SYTO16 and SYTOX Blue for live and dead cells, respectively (Figure 4H, right). The P1 subpopulation of small cells contains expelled nuclei (SYTO16^{high}) and enucleated reticulocytes (SYTO16^{low}) (Figure 4H, right), while the P2 population of larger cells consists of nucleated erythroblasts (SYTO16^{high}) with no enucleated SYTO19^{low} cells (not shown). The SYTOX Blue^{high} cells are dead (not shown) (Yoshida *et al.*, 2005). This analysis identified an increased percentage of enucleated cells (reticulocytes) only in the P1 subpopulation in *Tpm3/9d*$^{-/-}$ spleen but no changes in the either the P1 or P2 populations in *Tpm3/9d*$^{-/-}$ bone marrow (Figure 4, I and J), indicative of increased reticulocyte production due to increased splenic but not bone marrow erythropoiesis. Collectively these findings indicate that *Tpm3/9d*$^{-/-}$ mice undergo splenic stress erythropoiesis of sufficient magnitude to produce a fully compensated anemia. Thus the absence of Tpm3.1 with substitution by Tpm1.9 does not appear to affect erythroblast differentiation and RBC biogenesis.

Absence of Tpm3.1 results in abnormal RBC shapes and compromised mechanical properties

To ascertain the cellular mechanisms whereby the switch from equimolar Tpm1.9/Tpm3.1 in wild-type RBCs to exclusively Tpm1.9 in Tpm3.1-null RBCs leads to compensated anemia in *Tpm3/9d*$^{-/-}$ mice, we examined the shapes and mechanical properties of Tpm3.1-null RBCs. Blood smears revealed that Tpm3.1-null RBCs were more morphologically heterogeneous than wild-type RBCs, with appearance of microcytic, spherocytic, and mildly ovalocytic RBCs (Figure 5A). This morphological heterogeneity was also evidenced by an elevated RBC distribution width in the hematological analyses (Table 1) and by three-dimensional reconstructions of RBC shapes from confocal Z-stacks of Ter119-stained RBCs (Figure 5, B and C). Confocal Z-stacks also confirmed that Tpm3.1-null RBCs are abnormally spherocytic, based on high-resolution morphometric analysis of RBC thickness at the dimple versus periphery

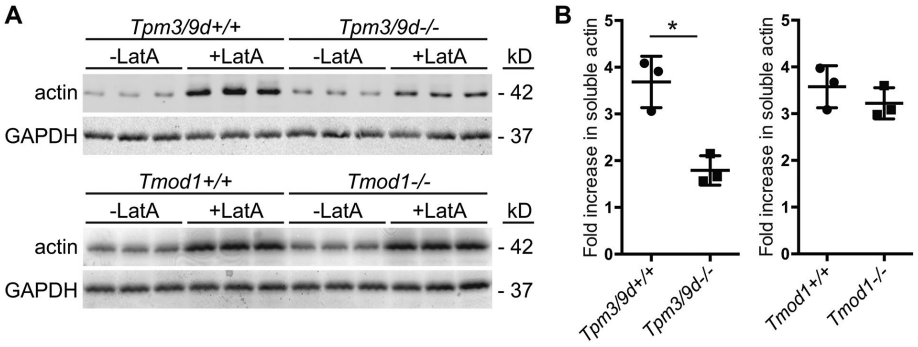

FIGURE 3: LatA-induced increases in soluble actin are attenuated in Tpm3.1-null RBCs but unaffected in Tmod1-null RBCs. (A) Western blots of Triton X-100–extracted RBC supernatants prepared from intact RBCs collected from *Tpm3/9d*$^{+/+}$, *Tpm3/9d*$^{-/-}$, *Tmod1*$^{+/+}$, and *Tmod1*$^{-/-}$ mice and treated with DMSO (-LatA) or DMSO with LatA (+LatA). Lanes represent RBC samples from individual mice. (B) Fold increase in GAPDH-normalized actin levels determined by densitometry of the blots in A. *$p < 0.05$.

(Figure 5, D and E). Quantification of maximum RBC diameters revealed that both wild-type and Tpm3.1-null RBCs had an identical average diameter of ~6 µm, but the diameters of Tpm3.1-null RBCs had markedly greater variance ($F = 2.25$; Figure 5F), with many Tpm3.1-null RBCs appearing elongated (ovalocytic; Figure 5C). The increased sphericity of Tpm3.1-null RBCs is associated with a small decrease in average surface area (Figure 5G), which is consistent with Tpm3.1-null RBCs having unchanged mean corpuscular volume (MCV; Table 1), since a less-flattened geometry minimizes the surface area required to enclose a fixed volume. The abnormal spherocytic and ovalocytic shapes of Tpm3.1-null RBCs are also associated with elevated corpuscular hemoglobin (total and concentration; Table 1) and slightly elevated osmotic fragility (Figure 6A), characteristic of the decreased surface-area-to-volume ratio of spherocytic RBCs (Mohandas and Chasis, 1993) and similar to findings in human hereditary spherocytosis patients (Cynober *et al.*, 1996; Michaels *et al.*, 1997). The spherocytosis-like phenotype of Tpm3.1-null RBCs may reflect weakened associations of Band 3 and GPA with the membrane skeleton (Figure 2), similar to phenotypes of other mutant RBCs with defective linkages between transmembrane glycoproteins and the membrane skeleton (Mohandas and Gallagher, 2008; Gallagher, 2013).

Finally, we tested whether the abnormal morphology of Tpm3.1-null RBCs is associated with altered biomechanical properties by analyzing RBC membrane deformability and stability using ektacytometry, a technique that monitors RBC membrane properties with increasing fluid shear stress (Mohandas *et al.*, 1982). These experiments showed that the maximum deformability index (DI) measured at 150 dynes/cm^2 is significantly decreased in Tpm3.1-null RBCs (Figure 6B). As the maximum DI directly reflects the membrane surface area (Clark *et al.*, 1983; Chasis and Mohandas, 1986), this confirms the membrane loss indicated by increased osmotic fragility of Tpm3.1-null RBCs (Figure 6A) and the presence of spherocytic cells in blood smears (Figure 5A). Next we analyzed the rate of DI decrease at a constant applied shear stress of 750 dynes/cm^2, which reflects RBC resistance to membrane fragmentation and vesiculation and, in turn, membrane stability (Mohandas *et al.*, 1982; Chasis and Mohandas, 1986). Unexpectedly, Tpm3.1-null RBCs had increased membrane stability in this assay (Figure 6C), unlike typical spherocytic RBCs, which have reduced membrane stability (Mohandas *et al.*, 1980; Chasis and Mohandas, 1986; Chasis *et al.*, 1988). Together these data suggest that F-actin hyperstability in RBCs containing exclusively Tpm1.9 is associated with increased membrane stability, while weakened Band 3 and GPA linkages to the membrane skeleton are associated with reduced surface area, leading to reduced deformability and increased osmotic fragility.

DISCUSSION

RBC tropomyosin isoform properties and mechanisms of isoform substitution

Short F-actins coated with Tpm1.9 and Tpm3.1 are key structural features of the RBC membrane skeleton. Here we show that Tpm3.1-null RBCs exhibit an unexpected compensatory increase of Tpm1.9, allowing Tpm3.1-null RBCs to maintain a total tropomyosin level comparable to wild-type RBCs, with no alterations in the composition of the membrane skeleton. However, the switch

	Tpm3/9d$^{+/+}$ (*n* = 5)	*Tpm3/9d*$^{-/-}$ (*n* = 5)
RBC count (× 10^6 cells/ml)	9.61 ± 0.27	9.65 ± 0.14
Hemoglobin concentration (g/dl)	14.14 ± 0.39	14.62 ± 0.30
Hematocrit (%)	42.12 ± 1.10	42.84 ± 0.91
Mean corpuscular volume (fl)	44.00 ± 0.00	44.40 ± 0.40
Mean corpuscular hemoglobin (pg)	14.72 ± 0.09	15.16 ± 0.14*
Mean corpuscular hemoglobin concentration (g/dl)	33.56 ± 0.15	34.16 ± 0.10*
RBC distribution width (%)	16.56 ± 0.11	17.78 ± 0.30**
Leukocyte count (× 10^3 cells/ml)	2.56 ± 0.53	1.58 ± 0.32
Platelet count (× 10^3 cells/ml)	755.00 ± 40.47	764.60 ± 76.64
Reticulocytes (%)	4.08 ± 0.22	5.04 ± 0.32*
Spleen weight (% of body weight)	0.29 ± 0.018	0.33 ± 0.017

Values are means ± SD. *, $p < 0.05$; **, $p < 0.01$.

TABLE 1: Hematological analysis of 2-mo-old male *Tpm3/9d*$^{+/+}$ and *Tpm3/9d*$^{-/-}$ mice.

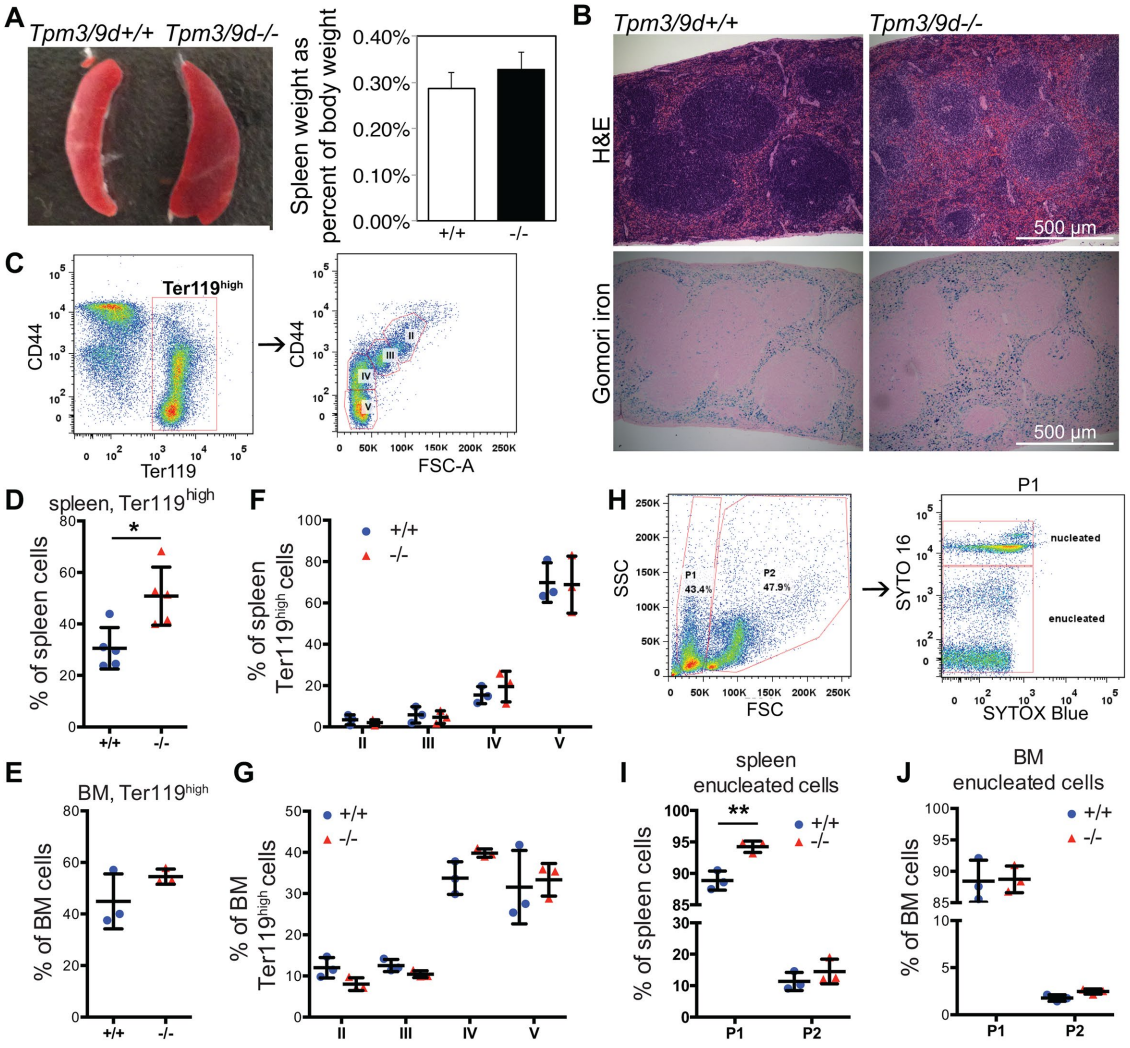

FIGURE 4: *Tpm3.1/9d*$^{-/-}$ mice exhibit a stress erythropoiesis response with increased splenic erythroblasts. (A) Left, *Tpm3.1/9d*$^{-/-}$ mouse spleen is slightly larger and redder than a *Tpm3.1/9d*$^{+/+}$ spleen. Right, spleen weights in 2-mo-old *Tpm3/9d*$^{+/+}$ and *Tpm3/9d*$^{-/-}$ male mice. A small increase was observed in *Tpm3/9d*$^{-/-}$ spleens but did not achieve statistical significance. $p = 0.098$; $n = 5$ spleens/genotype. (B) H&E staining of spleen sections reveals a greater proportion of red pulp areas positive for Gömöri iron staining in *Tpm3/9d*$^{-/-}$ mice as compared with *Tpm3/9d+/+* mice. Scale bar, 500 µm. (C) Representative flow cytometry profiles of splenic erythroblasts labeled with anti-CD44 and anti-Ter119 (left) and sorted for CD44 and forward light scatter (FSC-A) (right). Erythroblast populations at different stages of terminal differentiation are labeled II–V as in Chen *et al.*, (2009) and represent basophilic (early), polychromatic (intermediate), orthochromatic (late), or orthrochromatic erythroblasts plus reticulocytes and mature RBCs. (D, E) Percentage of Ter119^{high} erythroblasts in (D) spleen and (E) bone marrow, expressed as a percentage of total viable cells. Ter119^{high} erythroblasts are increased in spleen but not bone marrow, consistent with stress erythropoiesis. (F, G) Percentage of Ter119^{high} cells present in II, III, IV, and V populations from (F) spleen and (G) bone marrow from *Tpm3/9d*$^{+/+}$ and *Tpm3/9d*$^{-/-}$ mice. (H) Left, representative flow cytometry of spleen cells labeled with cell-permeable (SYTO16) and cell-impermeable (SYTOX Blue) DNA-staining dyes, analyzed by side light scatter (SSC) and forward light scatter (FSC). Right, events in the FSC^{low} P1 population (small cells) are shown for SYTO16 and SYTOX Blue, which contain expelled nuclei (SYTO16^{high}, SYTOX Blue^{low}), enucleated reticulocytes, and RBCs (SYTO16^{low}, SYTOX Blue^{low}), as shown previously (Yoshida *et al.*, 2005). The FSC^{high} P2 population (large cells) contains earlier-stage nucleated erythroblasts (SYTO16^{high}, SYTOX Blue^{low}; data not shown). (I, J) Percentage of P1 or P2 populations of enucleated cells in (I) spleen or (J) bone marrow from *Tpm3/9d*$^{+/+}$ and *Tpm3/9d*$^{-/-}$ mice. An increase in enucleated cells is observed in the P1 population from the spleen but not bone marrow, consistent with an increased rate of splenic erythropoiesis. *, $p < 0.05$; **, $p < 0.01$; $n = 3$ mice/genotype; BM, bone marrow.

from equimolar Tpm1.9/Tpm3.1 to exclusively Tpm1.9 causes RBC F-actins to become abnormally resistant to depolymerization, consistent with Tpm1.9's approximately twofold stronger affinity for F-actin and enhanced efficacy at reducing F-actin depolymerization in vitro (Yamashiro *et al.*, 2014). Moreover, Tpm1.9 interacts with Tmod1 more strongly than Tpm3.1 in solid-phase binding assays (Sung *et al.*, 2000), suggesting that Tpm1.9 is more effective than Tpm3.1 at anchoring Tmod1 onto the pointed end, providing further inhibition of F-actin depolymerization. Thus the Tpm3.1-null RBCs provide a cellular example of how a simple isoform swap

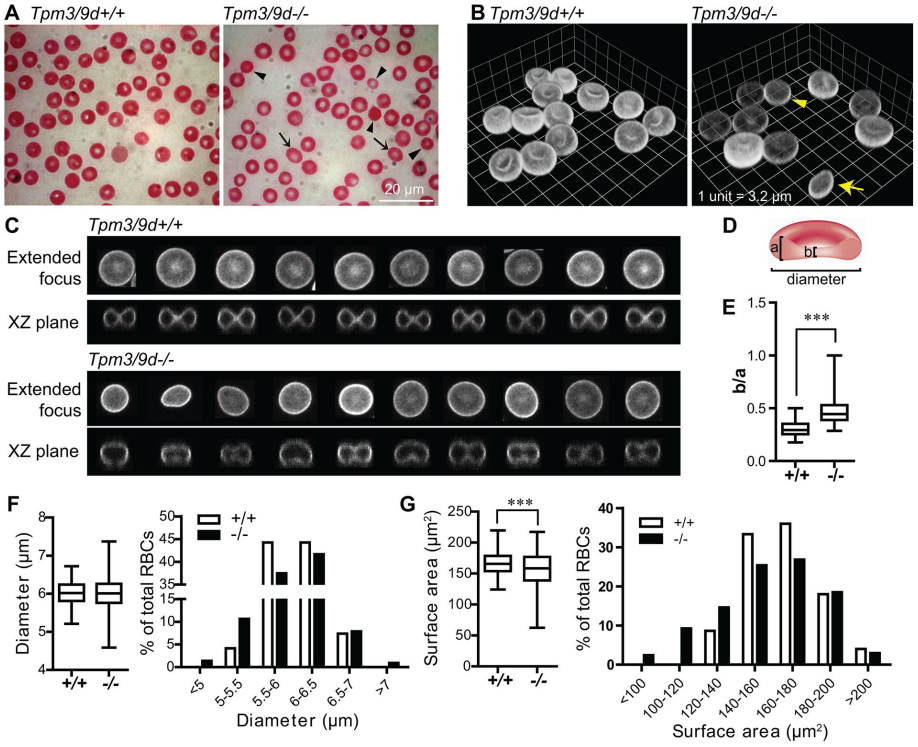

FIGURE 5: Tpm3.1-null RBCs exhibit abnormal spherocytic and ovalocytic morphologies. (A) Wright-Giemsa–stained blood smears from 2- to 3-mo-old *Tpm3/9d*$^{+/+}$ and *Tpm3/9d*$^{-/-}$ mice, showing that Tpm3.1-null RBCs have variable sizes and morphologies, with spherocytes and microcytes (arrowheads) and ovalocytes (arrows). Scale bar, 20 µm. (B) Three-dimensional reconstructions of confocal Z-stacks of Ter119-stained RBCs from *Tpm3/9d*$^{+/+}$ and *Tpm3/9d*$^{-/-}$ mice. Scale, 1 unit = 3.2 µm. (C) Confocal images (extended focus, top row; *xz*-plane, bottom row) of Ter119-stained RBCs from *Tpm3/9d*$^{+/+}$ and *Tpm3/9d*$^{-/-}$ mice. Wild-type RBCs are biconcave with the top and the bottom membrane appearing to make contact at this resolution (due to confocal Z-stretch). In Tpm3.1-null RBCs, the top and bottom membranes are further apart, leading to reduced biconcavity. (D) Diagram illustrating how RBC biconcavity was quantified by measuring the thickness at the rim (a) and at the center (b). (E) Biconcavity (b/a) of wild-type and Tpm3.1-null RBCs, measured from *xz*-plane images in C. Most Tpm3.1-null RBCs are thicker in the center, as indicated by elevated mean, and some are much thicker, indicated by the long upper tail of the box-and-whisker plot showing the top quartile. Wild type, $n = 80$ RBCs; Tpm3.1-null, $n = 92$ RBCs. (F) Maximum diameters of wild-type and Tpm3.1-null RBCs measured from extended-focus images in C. Left, box-and-whisker plot; right, histogram. There was no significant change in the average diameter of Tpm3.1-null RBCs, but diameters were more variable. Wild type, $n = 218$ RBCs; Tpm3.1-null, $n = 215$ RBCs. (G) Surface areas of wild-type and Tpm3.1-null RBCs measured from three-dimensional images in B. Left, box-and-whisker plot; right, histogram. Tpm3.1-null RBCs had smaller and more variable surface areas than wild-type RBCs. Wild type, $n = 150$ RBCs; Tpm3.1-null, $n = 205$ RBCs. RBCs from two mice/genotype were measured for all parameters. ***, $p < 0.001$.

from a low affinity Tpm3.1 to a high-affinity Tpm1.9 leads to a significant functional phenotype in vivo, without confounding effects due to altered tropomyosin levels characteristic of overexpression or knockdown approaches.

Because circulating RBCs lack the transcriptional machinery to up-regulate *Tpm1*, we speculate that Tpm1.9 levels are increased in Tpm3.1-null erythroblast progenitors, and excess Tpm1.9 is then recruited to the nascent membrane skeleton during erythroblast differentiation and reticulocyte maturation to occupy tropomyosin-binding sites on F-actin that would otherwise contain Tpm3.1. Such a mechanism parallels the proposed mechanism for how Tmod3 partially compensates for the absence of Tmod1 at the pointed ends of F-actins in Tmod1-null RBCs (Moyer *et al.*, 2010). Notably, tropomyosin isoform compensation by increased expression of other *Tpm* gene products is not observed in *Tpm3/9d*$^{-/-}$ neurons or fibroblasts (Fath *et al.*, 2010; Lees *et al.*, 2013) or in tumor cells in which Tpm3.1 function is blocked by a small-molecule inhibitor (Stehn *et al.*, 2013). Moreover, *Tpm3/9d*$^{-/-}$ neurons and fibroblasts exhibit altered splicing with expression of exon 9c of *Tpm3* (Tpm3.4/7) (Fath *et al.*, 2010), which we do not observe in *Tpm3/9d*$^{-/-}$ RBCs, suggesting that the isoform compensation mechanism observed in RBCs from *Tpm3/9d*$^{-/-}$ mice may be erythroid-specific. Additional studies are required to delineate the transcriptional circuitry and developmental timing of tropomyosin isoform expression and isoform compensation during erythroid differentiation.

The isoform switch observed in Tpm3.1-null RBCs, in which Tpm1.9 is increased so total tropomyosin levels are unchanged and the membrane skeleton is intact, is also a unique phenotype when placed in the broader context of studies examining the effects of nonmuscle tropomyosin isoform disruption on the F-actin cytoskeleton in other cell types. For example, in budding yeast, two tropomyosin isoforms, Tpm1p and Tpm2p, are present but have unequal abundances, with Tpm1p approximately sixfold more abundant than Tpm2p (Drees *et al.*, 1995). Deletion of Tpm1p results in disappearance of F-actin cables, resulting in defective vesicular trafficking (Liu and Bretscher, 1989), indicating that one yeast tropomyosin isoform cannot functionally compensate for the absence of the other. Analogous mechanisms (i.e., nonmuscle tropomyosin disruption leading to destabilization of F-actin–based structures with associated functional defects but no compensation by other *Tpm* genes) have also been observed in mammalian cells, including neurons (Fath *et al.*, 2010), fibroblasts (Lees *et al.*, 2013), skeletal myocytes (Vlahovich *et al.*, 2009), and adipocytes (Kee *et al.*, 2015). Why might the phenotype of Tpm3.1-null RBCs diverge from this pattern? One possibility is that RBCs lack a transcellular cytoskeleton, and the RBC F-actin network consists of only the short F-actins in the membrane skeleton. Assembly of short RBC F-actins might be less sensitive to tropomyosin isoform properties compared with assembly of longer, transcellular F-actin–based structures, allowing Tpm1.9 isoform compensation in Tpm3.1-null RBCs to preserve normal membrane skeleton assembly while enhancing F-actin stability, which may matter only in mature RBCs.

Tropomyosin function in RBC F-actin regulation

Tpm3.1-null RBCs, which show compensatory appearance of Tpm1.9, exhibit increased F-actin stability in response to LatA-induced depolymerization, yet Tmod1-null RBCs, which show compensatory appearance of Tmod3 at only ~20% of wild-type levels (Moyer *et al.*, 2010), exhibit normal F-actin stability. We previously

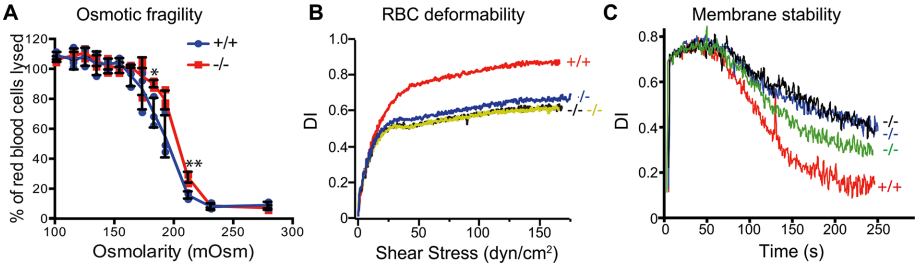

FIGURE 6: Tpm3.1-null RBCs exhibit abnormal biomechanical properties. (A) Osmotic fragility curves for RBCs from 2-mo-old *Tpm3/9d*$^{+/+}$ and *Tpm3/9d*$^{-/-}$ mice. $n = 3$ mice/genotype. The curve shows a small rightward shift for Tpm3.1-null RBCs, reflecting osmotic fragility consistent with a mild spherocytosis. *, $p < 0.05$; **, $p < 0.01$. (B) RBC deformability curves for RBCs from 3-mo-old *Tpm3/9d*$^{+/+}$ and *Tpm3/9d*$^{-/-}$ mice generated by progressively increasing shear stress. Deformability index (DI) is reduced in in Tpm3.1-null RBCs. (C) Mechanical stability curves for resealed ghosts from 2-mo-old *Tpm3/9d*$^{+/+}$ and *Tpm3/9d*$^{-/-}$ mice. Tpm3.1-null RBCs exhibit resistance to fragmentation (smaller reduction in DI) over time at high shear stresses, indicative of increased membrane mechanical stability. A representative trace is shown for RBCs from one *Tpm3/9d*$^{+/+}$ mouse (B, C, red), and individual traces are shown for RBCs from three *Tpm3/9d*$^{-/-}$ mice (B, black, blue, yellow; C, black, blue, green). $n = 3$ mice/genotype.

showed that F-actins from Tmod1-null RBCs have markedly more variable lengths, with emergence of a subpopulation of shorter F-actins that likely lack tropomyosin and another subpopulation of longer F-actins that are likely two tropomyosins long and capped by Tmod3 (Moyer *et al.*, 2010). Moreover, in striated muscle sarcomeres, antibody inhibition of Tmod1's pointed-end capping activity or RNAi depletion of Tmod1 protein levels does not destabilize thin filaments (i.e., lead to their depolymerization) but rather results in longer thin filaments (Gregorio *et al.*, 1995; Gokhin *et al.*, 2015b). In contrast, antibody inhibition of tropomyosin-Tmod1 binding or introduction of the nemaline myopathy-causing *TPM3*-R167H mutation shortens thin filaments, suggesting actin filament destabilization (Mudry *et al.*, 2003; Ochala *et al.*, 2012). By integrating these findings, we propose a model whereby RBC tropomyosins and Tmod1 influence RBC F-actin architecture via two complementary mechanisms. First, equimolar Tpm1.9 and Tpm3.1 synergize to provide finely tuned inhibition of F-actin shortening, as determined by the combination of these isoforms' F-actin-binding and Tmod1-binding affinities. Second, Tmod1 inhibits F-actin elongation, as determined by its pointed-end capping activity for Tpm1.9/Tpm3.1-coated F-actin and binding affinity for Tpm1.9 and Tpm3.1. This precise balance of "shortening-inhibition" and "elongation-inhibition" signals may account for how uniform RBC F-actin lengths are maintained over the lifespan of a circulating RBC.

Tropomyosin function in RBC cytoarchitecture and membrane physiology

We made the unexpected discovery that the switch from equimolar Tpm1.9/Tpm3.1 in wild-type RBCs to exclusively Tpm1.9 in Tpm3.1-null RBCs leads to decreased association of Band 3 and GPA with the membrane skeleton, without affecting the composition of the membrane skeleton. This reveals a novel mechanism for regulation of "vertical interactions" between the membrane skeleton and transmembrane glycoproteins, as shown previously for F-actin-to-membrane vertical interactions mediated by αβ-adducin and protein 4.1R (Pasternack *et al.*, 1985; Anong *et al.*, 2009). Additional biochemical experiments and analyses of *Tpm3/9d*$^{-/-}$ mice are needed to fully elucidate the nature of tropomyosin regulation of membrane skeleton-glycoprotein connectivity by determining 1) whether tropomyosin directly binds to transmembrane glycoproteins or whether as-yet-unknown molecular linkages indirectly mediate tropomyosin's effects; 2) whether tropomyosin is involved in establishing membrane skeleton-glycoprotein linkages to target membrane glycoproteins to the bilayer during erythroblast differentiation and reticulocyte maturation; and 3) whether tropomyosin stabilizes membrane skeleton-glycoprotein linkages to prevent glycoprotein and membrane loss during the lifespan of the circulating RBC.

The switch from equimolar Tpm1.9/Tpm3.1 to exclusively Tpm1.9, with the concomitant increase in RBC F-actin stability and weakening of linkages between the membrane skeleton and transmembrane glycoproteins, leads to abnormal spherocytic and ovalocytic RBC morphologies, increased osmotic fragility, and reduced membrane deformability but increased mechanical stability in response to shear stresses. The spherocytic morphologies and reduced deformability of Tpm3.1-null RBCs imply a reduced surface-area-to-volume ratio (Mohandas and Gallagher, 2008), which is reflected by impaired osmotic fragility. However, mouse knockouts and human patients with spherocytic RBCs have reduced deformability and reduced mechanical stability (Mohandas and Gallagher, 2008), unlike the Tpm3.1-null mouse RBCs, where these properties are uncorrelated.

We propose three nonmutually exclusive mechanisms to account for the observed Tpm3.1-null RBC phenotypes: 1) Weakened Band 3 and GPA associations with the membrane skeleton may result in insufficient vertical connectivity, leading to the observed spherocytosis-like phenotype and associated biomechanical defects, including reduced deformability and increased osmotic fragility. 2) Increased F-actin stability may reflect a reduced rate of G-actin subunit association/dissociation at RBC F-actin ends, reducing the rate of $(\alpha_1\beta_1)_2$-spectrin association/dissociation with F-actin (Gov and Safran, 2005; Li *et al.*, 2007), thereby enhancing "horizontal interactions." This may attenuate the long-range plasticity of the $(\alpha_1\beta_1)_2$-spectrin lattice, which may manifest as abnormal RBC shapes and reduced membrane extensibility (deformability), along with increased membrane mechanical stability. 3) Increased F-actin stability may indirectly strengthen F-actin–based vertical interactions, possibly by promoting the interaction of αβ-adducin with Band 3 (Anong *et al.*, 2009) or the interactions of Band 4.1R with glycophorin-C and Band 3 (Anderson and Lovrien, 1984; Pasternack *et al.*, 1985; Marfatia *et al.*, 1994). Mice lacking α- or β-adducin exhibit reduced levels of RBC tropomyosins along with fragile and spheroelliptocytic RBCs (Gilligan *et al.*, 1999; Muro *et al.*, 2000; Porro *et al.*, 2004; Robledo *et al.*, 2008), suggesting functional interactions among these RBC F-actin binding proteins, although, to date, there is no evidence for direct binding among them. Functional interactions among RBC F-actin-binding proteins are also supported by observations in dematin-null RBCs, which exhibit dramatically reduced levels of $(\alpha_1\beta_1)_2$-spectrin, αβ-adducin, and actin (Lu *et al.*, 2016).

MATERIALS AND METHODS

Mice, genotyping, and blood collection

Generation of *Tpm3/9d*$^{-/-}$ mice was described previously (Fath *et al.*, 2010; Hook *et al.*, 2011; Lees *et al.*, 2013). The presence of wild-type and mutant *Tpm3* alleles was confirmed by automated

qPCR genotyping of tail-snip biopsies (Transnetyx, Cordova, TN). *Tmod1*$^{-/-}$ mice were generated and maintained as previously described (McKeown *et al.*, 2008; Moyer *et al.*, 2010). Adult (2–4-mo-old) mice were killed by isoflurane inhalation followed by cervical dislocation. Blood was isolated by cardiac puncture into BD Vacutainer K_3EDTA purple-top blood collection tubes. All experiments were performed according to National Institutes of Health (NIH) animal care guidelines, as approved and enforced by the Institutional Animal Care and Use Committee at The Scripps Research Institute.

Ghost preparation and Western blotting

Aliquots (125 µl) of whole blood from each mouse were distributed to 1.5-ml microfuge tubes, RBCs were isolated by sedimentation through 0.75% Dextran T500 to remove leukocytes, and RBCs were washed 4× in phosphate-buffered saline (PBS; 10 mM $NaHP0_4$, pH 7.4, 150 mM NaCl) at 4°C (Moyer *et al.*, 2010). Ghosts were prepared from RBC pellets by hypotonic lysis in ~20 volumes ice-cold Mg^{2+}-lysis buffer, as described previously (Moyer *et al.*, 2010), and either used immediately or stored at -80°C until use. Membrane skeletons were prepared from ghost pellets by extraction with ~20 volumes of 2% Triton X-100 in ice-cold lysis buffer (Moyer *et al.*, 2010). Gel samples of ghosts were prepared by the addition of an equal volume of 5× SDS sample buffer and boiling for 5 min. Membrane skeleton pellets were resuspended to the original ghost volume and solubilized as above. Proteins were separated on 7.5–15% linear gradient mini-gels (Figures 1 and 3) (Life Technologies) or 4.0–20% linear gradient mini-gels (Figure 2) (Invitrogen), and either stained with Coomassie blue (1-Step Blue, Biotium) or transferred to nitrocellulose membranes for Western blotting in a standard 20% methanol Tris-glycine buffer (150 V, 2 h at 4°C). Transfers were preheated for 1 h at 65°C in PBS, stained in Ponceau S and scanned for total protein, followed by blocking in 4% bovine serum albumin (BSA) (Pentex Fraction V) in PBS for 2 h at room temperature (RT). Transfers were then incubated in primary antibodies in 4% BSA, 0.1% Triton X-100 in PBS overnight at 4°C, or 4 h at RT, followed by washing in the same buffer without BSA and then labeled with secondary antibodies in 4% BSA, 0.1% Triton X-100 in PBS for 1 h at RT before final washes and detection by chemiluminescence or infrared imaging (see below).

Primary tropomyosin antibodies were as described in Schevzov *et al.* (2011) as follows: sheep anti–Tpm3/exon-9d (AB5447; EMD Millipore), sheep anti–Tpm1/exon-9d (AB5441; EMD Millipore), rabbit anti-Tpm4.2 (AB5449; EMD Millipore), and mouse anti-muscle tropomyosin (TM311; Abcam). Other primary antibodies were as follows: mouse monoclonal anti–pan-actin (C4, 1:10,000; EMD Millipore), rabbit anti–Band 3 (a gift from L. L. Peters, Jackson Laboratories, Bar Harbor, ME), rabbit anti-mouse glycophorin A and anti-mouse glycophorin C (Salomao *et al.*, 2008), rabbit anti–Band 4.1R (a gift from Cathy Korsgren and Samuel Lux, Boston Children's Hospital, Boston, MA), affinity-purified chicken anti–α- and β-adducin (a gift from Diana Gilligan, Upstate University Hospital, Syracuse, NY) (Moyer *et al.*, 2010), rabbit anti-dematin (a gift from A. H. Chishti, Tufts University School of Medicine, Boston, MA), mouse monoclonal anti–glyceraldehyde 3-phosphate dehydrogenase (GAPDH) (1D4, 1:5000; Novus Biologicals), anti-rabbit GAPDH (SC25778; Santa Cruz Biotechnologies), rabbit affinity-purified anti-human Tmod1 (cross-reacts with mouse Tmod1) (R1749bl3c) (Fowler *et al.*, 1993), or anti-Tmod1 C-terminal peptide antibody (PA2211; Gokhin *et al.*, 2012). For Figure 1, secondary antibodies were horseradish peroxidase (HRP)-conjugated goat anti-mouse immunoglobulin G (IgG) (Promega), HRP-goat anti-rabbit IgG (Santa Cruz Biotechnologies), and HRP-rabbit anti-sheep IgG (Life Technologies). For Figures 2 and 3, secondary antibodies were LI-COR IRDye 680LT- or 800CW-conjugated anti-mouse, anti-rabbit, anti-chicken, or anti-sheep IgGs, as appropriate. Bands were visualized by enhanced chemiluminescence (Figure 1) or a LI-COR Odyssey infrared imaging system (Figures 2 and 3), and background-corrected band intensities were densitometrically quantified with ImageJ software (https://imagej.nih.gov/ij/). Western band intensities were normalized to that of GAPDH or to total protein by Ponceau S staining, as indicated.

RBC F-actin stability assay

F-actin stability in washed intact RBCs was assessed as described previously (Gokhin *et al.*, 2015a). Briefly, RBCs were washed into HEPES-buffered saline, resuspended to approximately a 10% cell suspension (vol/vol), and incubated in 10-µm LatA in dimethyl sulfoxide (DMSO) (Sigma-Aldrich) for 4 h in a 37°C shaking water bath. RBCs were then extracted by the addition of four volumes Triton-lysis buffer containing 2.5% Triton X-100, and supernatants (soluble fractions) were separated from pellets (membrane skeleton fractions) by centrifugation of membrane skeletons through a sucrose shelf. Soluble fractions were solubilized in 1/5 vol of 5 × SDS sample buffer, and cytosolic G-actin was detected by Western blotting, as described above (Gokhin *et al.*, 2015a).

Hematology, osmotic fragility, and ektacytometry of RBCs

Whole mouse blood was collected from 2-mo-old male mice as described above, and complete blood counts were obtained using a scil Vet ABC hematology analyzer (scil animal care, Gurnee, IL) calibrated for mouse blood. Osmotic fragility was performed on RBCs from 2-mo-old male mice as previously described (Gilligan *et al.*, 1999), and ektacytometry was performed on RBCs from 3-mo-old male mouse blood stored overnight at 4°C (Chasis and Mohandas, 1986). Briefly, to assess membrane deformability, 25 µl RBCs were suspended in 4 ml of 3% polyvinylpyrrolidone and exposed to an increasing shear stress (0–150 dynes/cm^2) in an ektacytometer. To assess membrane mechanical stability, resealed ghosts were suspended in 45% dextran and exposed to a constant applied shear stress of 750 dynes/cm^2.

Histology

Spleens were fixed overnight in 10% Formalin, paraffin embedded, sectioned, and stained with either H&E for routine histologic examination or Gömöri iron stain with Nuclear Fast Red counterstain for detection of hemoglobin. Peripheral blood smears were stained with Wright-Giemsa. Samples were photographed on a Zeiss Axioskop bright-field microscope using a 100× objective oil lens (N.A. 1.4) and a Zeiss Axiocam charged-coupled-device camera.

Fluorescence confocal microscopy for RBC shape measurements

RBCs were fixed by a 50- to 100-fold dilution of whole blood into PBS containing 4% paraformaldehyde (PFA) with 0.05% glutaraldehyde and incubated overnight at RT. After washing RBCs 3 × in PBS, nonspecific binding sites were blocked for at least 2 h at RT in 2% BSA + 0.1% Triton X-100 in PBS (PBST). RBCs were stained with Alexa Fluor 488-conjugated anti-Ter119 (1:100, BioLegend) in PBST for 2 h at RT, washed 3× in PBST, and deposited onto coverslips using a Thermo-Fisher Cytospin 4 at 900–1000 rpm for 3 min. Coverslips were mounted on slides using Fluoro-Gel aqueous mounting medium (Electron Microscopy Sciences, Hatfield, PA), and 3D

Z-stacks were acquired on a Zeiss LSM780 laser-scanning confocal fluorescence microscope using a Zeiss 100 × oil-immersion objective (N.A. 1.4). Images were reconstructed with Volocity 6.3 software (Perkin Elmer-Cetus), and maximum diameters, surface areas, and volumes were measured in Volocity.

Immunofluorescence staining and TIRF microscopy

RBCs were isolated from blood by washing 3 × in PBS, resuspended to ~2 × 10^6 cells/ml in PBS, and adhered for 30 min at RT to a glass coverslip–bottomed dish (FluoroDish FD35-100, World Precision Instruments) coated with high-molecular-weight 0.1% poly-L-lysine in water (Sigma-Aldrich; P8920). Adherent cells were fixed in 4% PFA in PBS for 4 h at RT, washed 3 × in PBS, permeabilized in 0.3% Triton X-100 in PBS for 10 min at RT, and blocked overnight at 4°C in 3% BSA + 10% donkey serum in PBS. Cells were stained for 2–3 h at RT with primary antibodies to Tpm3.1 (1:100 sheep anti–Tpm3/exon-9d, AB5447; EMD Millipore), or Tpm1.9 (1:100 sheep anti–Tpm1/exon-9d, AB5441; EMD Millipore) in 2% BSA + 10% donkey serum in PBS, washed 3 × in PBS, and stained for 2 h at RT with Alexa-488-conjugated donkey anti-sheep secondary antibodies (1:500; Invitrogen) along with rhodamine-phalloidin (1:200; Life Technologies) to stain F-actin in 2% BSA + 10% donkey serum in PBS. After three washes in PBS, cells were observed as wet mounts using total internal reflection fluorescence (TIRF) microscopy to selectively image the membrane interface. Images were acquired on a Nikon Eclipse Ti inverted microscope with a 100×Apochromat oil objective (N.A. 1.49), using TIRF illumination with 488 and 561 laser lines and an ORCA-Flash 4.0 V2 Digital complementary metal–oxide–semiconductor camera (Hamamatsu). Images were acquired using NIS-Elements 4.1 software (Nikon, Melville, NY) and processed using Volocity 6.3 software (Perkin Elmer-Cetus).

Flow cytometry

Spleens and bone marrows were dissected, and cells were triturated with a 1-ml serological pipette and passed through a 70-μm cell strainer (BD Biosciences). To analyze erythroblast differentiation, cells were stained with allophycocyanin-conjugated rat anti-mouse CD44 (BD Biosciences) and FITC-conjugated rat anti-mouse Ter119 BD Biosciences; Kina *et al.*, 2000), as previously described (Chen *et al.*, 2009). To analyze enucleation, cells were stained with SYTO16 and SYTOX Blue (Molecular Probes, Eugene, OR), as previously described (Yoshida *et al.*, 2005). To quantify reticulocytes, whole blood was stained with a BD Retic-Count Kit (BD Biosciences), according to the manufacturer's protocol. Flow cytometry was performed using a BD LSR II flow cytometer with BD FACSDiva software. Data were analyzed with FlowJo 9.2 software.

Statistical analysis

Data are presented as mean ± SD. Differences between means were detected using two-tailed unpaired Student's *t* tests, and differences between variances were detected using *F* tests. Statistical significance was defined as $p < 0.05$. Statistical analysis was performed using GraphPad Prism 5.0 software or Microsoft Excel 2011. Box-and-whisker plots show mean values (horizontal center line), quartiles immediately above and below the mean (top and bottom portions of boxes), and the minimum and maximum of the data (lower and upper quartiles; whiskers).

ACKNOWLEDGMENTS

We gratefully acknowledge Peter Gunning (University of New South Wales) for providing breeding pairs of *Tpm3/9d*$^{-/-}$ mice, Anita Sansoucie (The Scripps Research Institute) for assistance with histology, and Xin Du (University of California, San Diego) for use of her scil Vet ABC hematology analyzer. We also thank the reviewers for suggesting the experiments to investigate membrane glycoprotein levels in *Tpm3/9d*$^{-/-}$ ghosts and membrane skeletons. This work was supported by NIH/National Heart, Lung, and Blood Institute grant R01-HL083464 (to V.M.F.), NIH/National Institute of Diabetes and Digestive and Kidney Diseases grant R01-DK100810 (to X.A.), and NIH/National Institute of Arthritis and Musculoskeletal and Skin Diseases grant K99-AR066534 (to D.S.G.).

REFERENCES

An X, Salomao M, Guo X, Gratzer W, Mohandas N (2007). Tropomyosin modulates erythrocyte membrane stability. Blood 109, 1284–1288.

Anderson RA, Lovrien RE (1984). Glycophorin is linked by band 4.1 protein to the human erythrocyte membrane skeleton. Nature 307, 655–658.

Anong WA, Franco T, Chu H, Weis TL, Devlin EE, Bodine DM, An X, Mohandas N, Low PS (2009). Adducin forms a bridge between the erythrocyte membrane and its cytoskeleton and regulates membrane cohesion. Blood 114, 1904–1912.

Bennett V, Baines AJ (2001). Spectrin and ankyrin-based pathways: metazoan inventions for integrating cells into tissues. Physiol Rev 81, 1353–1392.

Bennett V, Healy J (2008). Organizing the fluid membrane bilayer: diseases linked to spectrin and ankyrin. Trends Mol Med 14, 28–36.

Bennett V, Lorenzo DN (2013). Spectrin- and ankyrin-based membrane domains and the evolution of vertebrates. Curr Top Membr 72, 1–37.

Broschat KO (1990). Tropomyosin prevents depolymerization of actin filaments from the pointed end. J Biol Chem 265, 21323–21329.

Broschat KO, Weber A, Burgess DR (1989). Tropomyosin stabilizes the pointed end of actin filaments by slowing depolymerization. Biochemistry 28, 8501–8506.

Chasis JA, Agre P, Mohandas N (1988). Decreased membrane mechanical stability and in vivo loss of surface area reflect spectrin deficiencies in hereditary spherocytosis. J Clin Invest 82, 617–623.

Chasis JA, Mohandas N (1986). Erythrocyte membrane deformability and stability: two distinct membrane properties that are independently regulated by skeletal protein associations. J Cell Biol 103, 343–350.

Chen K, Liu J, Heck S, Chasis JA, An X, Mohandas N (2009). Resolving the distinct stages in erythroid differentiation based on dynamic changes in membrane protein expression during erythropoiesis. Proc Natl Acad Sci USA 106, 17413–17418.

Clark MR, Mohandas N, Shohet SB (1983). Osmotic gradient ektacytometry: comprehensive characterization of red cell volume and surface maintenance. Blood 61, 899–910.

Cynober T, Mohandas N, Tchernia G (1996). Red cell abnormalities in hereditary spherocytosis: relevance to diagnosis and understanding of the variable expression of clinical severity. J Lab Clin Med 128, 259–269.

Da Costa L, Galimand J, Fenneteau O, Mohandas N (2013). Hereditary spherocytosis, elliptocytosis, and other red cell membrane disorders. Blood Rev 27, 167–178.

Drees B, Brown C, Barrell BG, Bretscher A (1995). Tropomyosin is essential in yeast, yet the TPM1 and TPM2 products perform distinct functions. J Cell Biol 128, 383–392.

Fath T, Agnes Chan YK, Vrhovski B, Clarke H, Curthoys N, Hook J, Lemckert F, Schevzov G, Tam P, Watson CM, *et al.* (2010). New aspects of tropomyosin-regulated neuritogenesis revealed by the deletion of Tm5NM1 and 2. Eur J Cell Biol 89, 489–498.

Fowler VM (1987). Identification and purification of a novel Mr 43,000 tropomyosin-binding protein from human erythrocyte membranes. J Biol Chem 262, 12792–12800.

Fowler VM (1990). Tropomodulin: a cytoskeletal protein that binds to the end of erythrocyte tropomyosin and inhibits tropomyosin binding to actin. J Cell Biol 111, 471–481.

Fowler VM (1996). Regulation of actin filament length in erythrocytes and striated muscle. Curr Opin Cell Biol 8, 86–96.

Fowler VM (2013). The human erythrocyte plasma membrane: a Rosetta Stone for decoding membrane-cytoskeleton structure. Curr Top Membr 72, 39–88.

Fowler VM, Bennett V (1984). Erythrocyte membrane tropomyosin: purification and properties. J Biol Chem 259, 5978–5989.

Fowler VM, Sussmann MA, Miller PG, Flucher BE, Daniels MP (1993). Tropomodulin is associated with the free (pointed) ends of the thin filaments in rat skeletal muscle. J Cell Biol 120, 411–420.

Fujime S, Ishiwata S (1971). Dynamic study of F-actin by quasielastic scattering of laser light. J Mol Biol 62, 251–265.
Gallagher PG (2013). Abnormalities of the erythrocyte membrane. Pediatr Clin North Am 60, 1349–1362.
Geeves MA, Hitchcock-DeGregori SE, Gunning PW (2015). A systematic nomenclature for mammalian tropomyosin isoforms. J Muscle Res Cell Motil 36, 147–153.
Gilligan DM, Lozovatsky L, Gwynn B, Brugnara C, Mohandas N, Peters LL (1999). Targeted disruption of the beta adducin gene (Add2) causes red blood cell spherocytosis in mice. Proc Natl Acad Sci USA 96, 10717–10722.
Gokhin DS, Fowler VM (2016). Feisty filaments: actin dynamics in the red blood cell membrane skeleton. Curr Opin Hematol 23, 206–214.
Gokhin DS, Kim NE, Lewis SA, Hoenecke HR, D'Lima DD, Fowler VM (2012). Thin-filament length correlates with fiber type in human skeletal muscle. Am J Physiol Cell Physiol 302, C555–C565.
Gokhin DS, Nowak RB, Khoory JA, de la Piedra A, Ghiran IC, Fowler VM (2015a). Dynamic actin filaments control the mechanical behavior of the human red blood cell membrane. Mol Biol Cell 26, 1699–1710.
Gokhin DS, Ochala J, Domenighetti AA, Fowler VM (2015b). Tropomodulin 1 directly controls thin filament length in both wild-type and tropomodulin 4-deficient skeletal muscle. Development 142, 4351–4362.
Gov NS, Safran SA (2005). Red blood cell membrane fluctuations and shape controlled by ATP-induced cytoskeletal defects. Biophys J 88, 1859–1874.
Grazi E, Cintio O, Trombetta G (2004). On the mechanics of the actin filament: the linear relationship between stiffness and yield strength allows estimation of the yield strength of thin filament in vivo. J Muscle Res Cell Motil 25, 103–105.
Greenfield NJ, Kostyukova AS, Hitchcock-DeGregori SE (2005). Structure and tropomyosin binding properties of the N-terminal capping domain of tropomodulin 1. Biophys J 88, 372–383.
Gregorio CC, Weber A, Bondad M, Pennise CR, Fowler VM (1995). Requirement of pointed-end capping by tropomodulin to maintain actin filament length in embryonic chick cardiac myocytes. Nature 377, 83–86.
Gunning PW, Hardeman EC, Lappalainen P, Mulvihill DP (2015). Tropomyosin—master regulator of actin filament function in the cytoskeleton. J Cell Sci 128, 2965–2974.
Hook J, Lemckert F, Schevzov G, Fath T, Gunning P (2011). Functional identity of the gamma tropomyosin gene: implications for embryonic development, reproduction and cell viability. Bioarchitecture 1, 49–59.
Kee AJ, Yang L, Lucas CA, Greenberg MJ, Martel N, Leong GM, Hughes WE, Cooney GJ, James DE, Ostap EM, *et al*. (2015). An actin filament population defined by the tropomyosin Tpm3.1 regulates glucose uptake. Traffic 16, 691–711.
Kina T, Ikuta K, Takayama E, Wada K, Majumdar AS, Weissman IL, Katsura Y (2000). The monoclonal antibody TER-119 recognizes a molecule associated with glycophorin A and specifically marks the late stages of murine erythroid lineage. Br J Haematol 109, 280–287.
Kojima H, Ishijima A, Yanagida T (1994). Direct measurement of stiffness of single actin filaments with and without tropomyosin by in vitro nanomanipulation. Proc Natl Acad Sci USA 91, 12962–12966.
Kostyukova AS (2008). Tropomodulin/tropomyosin interactions regulate actin pointed end dynamics. Adv Exp Med Biol 644, 283–292.
Kostyukova AS, Choy A, Rapp BA (2006). Tropomodulin binds two tropomyosins: a novel model for actin filament capping. Biochemistry 45, 12068–12075.
Kostyukova AS, Hitchcock-Degregori SE, Greenfield NJ (2007). Molecular basis of tropomyosin binding to tropomodulin, an actin-capping protein. J Mol Biol 372, 608–618.
Lees JG, Ching YW, Adams DH, Bach CT, Samuel MS, Kee AJ, Hardeman EC, Gunning P, Cowin AJ, O'Neill GM (2013). Tropomyosin regulates cell migration during skin wound healing. J Invest Dermatol 133, 1330–1339.
Lewis RA, Yamashiro S, Gokhin DS, Fowler VM (2014). Functional effects of mutations in the tropomyosin-binding sites of tropomodulin1 and tropomodulin3. Cytoskeleton (Hoboken) 71, 395–411.
Li J, Lykotrafitis G, Dao M, Suresh S (2007). Cytoskeletal dynamics of human erythrocyte. Proc Natl Acad Sci USA 104, 4937–4942.
Liu H, Bretscher A (1992). Characterization of TPM1 disrupted yeast cells indicates an involvement of tropomyosin in directed vesicular transport. J Cell Biol 118, 285–299.
Liu HP, Bretscher A (1989). Disruption of the single tropomyosin gene in yeast results in the disappearance of actin cables from the cytoskeleton. Cell 57, 233–242.
Lu Y, Hanada T, Fujiwara Y, Nwankwo JO, Wieschhaus AJ, Hartwig J, Huang S, Han J, Chishti AH (2016). Gene disruption of dematin causes precipitous loss of erythrocyte membrane stability and severe hemolytic anemia. Blood 128, 93–103.
Lux SE (2016). Anatomy of the red cell membrane skeleton: unanswered questions. Blood 127, 187–199.
Marfatia SM, Lue RA, Branton D, Chishti AH (1994). In vitro binding studies suggest a membrane-associated complex between erythroid p55, protein 4.1, and glycophorin C. J Biol Chem 269, 8631–8634.
Mattheyses AL, Simon SM, Rappoport JZ (2010). Imaging with total internal reflection fluorescence microscopy for the cell biologist. J Cell Sci 123, 3621–3628.
McKeown CR, Nowak RB, Moyer J, Sussman MA, Fowler VM (2008). Tropomodulin1 is required in the heart but not the yolk sac for mouse embryonic development. Circ Res 103, 1241–1248.
Michaels LA, Cohen AR, Zhao H, Raphael RI, Manno CS (1997). Screening for hereditary spherocytosis by use of automated erythrocyte indexes. J Pediatr 130, 957–960.
Mohandas N, Chasis JA (1993). Red blood cell deformability, membrane material properties and shape: regulation by transmembrane, skeletal and cytosolic proteins and lipids. Semin Hematol 30, 171–192.
Mohandas N, Clark MR, Health BP, Rossi M, Wolfe LC, Lux SE, Shohet SB (1982). A technique to detect reduced mechanical stability of red cell membranes: relevance to elliptocytic disorders. Blood 59, 768–774.
Mohandas N, Clark MR, Jacobs MS, Shohet SB (1980). Analysis of factors regulating erythrocyte deformability. J Clin Invest 66, 563–573.
Mohandas N, Evans E (1994). Mechanical properties of the red cell membrane in relation to molecular structure and genetic defects. Annu Rev Biophys Biomol Struct 23, 787–818.
Mohandas N, Gallagher PG (2008). Red cell membrane: past, present, and future. Blood 112, 3939–3948.
Moyer JD, Nowak RB, Kim NE, Larkin SK, Peters LL, Hartwig J, Kuypers FA, Fowler VM (2010). Tropomodulin 1-null mice have a mild spherocytic elliptocytosis with appearance of tropomodulin 3 in red blood cells and disruption of the membrane skeleton. Blood 116, 2590–2599.
Mudry RE, Perry CN, Richards M, Fowler VM, Gregorio CC (2003). The interaction of tropomodulin with tropomyosin stabilizes thin filaments in cardiac myocytes. J Cell Biol 162, 1057–1068.
Muro AF, Marro ML, Gajovic S, Porro F, Luzzatto L, Baralle FE (2000). Mild spherocytic hereditary elliptocytosis and altered levels of alpha- and gamma-adducins in beta-adducin-deficient mice. Blood 95, 3978–3985.
Ochala J, Gokhin DS, Penisson-Besnier I, Quijano-Roy S, Monnier N, Lunardi J, Romero NB, Fowler VM (2012). Congenital myopathy-causing tropomyosin mutations induce thin filament dysfunction via distinct physiological mechanisms. Hum Mol Genet 21, 4473–4485.
Pasternack GR, Anderson RA, Leto TL, Marchesi VT (1985). Interactions between protein 4.1 and band 3: an alternative binding site for an element of the membrane skeleton. J Biol Chem 260, 3676–3683.
Paulson RF, Shi L, Wu DC (2011). Stress erythropoiesis: new signals and new stress progenitor cells. Curr Opin Hematol 18, 139–145.
Pinder JC, Gratzer WB (1983). Structural and dynamic states of actin in the erythrocyte. J Cell Biol 96, 768–775.
Pollard TD, Blanchoin L, Mullins RD (2000). Molecular mechanisms controlling actin filament dynamics in nonmuscle cells. Annu Rev Biophys Biomol Struct 29, 545–576.
Porro F, Costessi L, Marro ML, Baralle FE, Muro AF (2004). The erythrocyte skeletons of beta-adducin deficient mice have altered levels of tropomyosin, tropomodulin and EcapZ. FEBS Lett 576, 36–40.
Rao JN, Madasu Y, Dominguez R (2014). Mechanism of actin filament pointed-end capping by tropomodulin. Science 345, 463–467.
Robledo RF, Ciciotte SL, Gwynn B, Sahr KE, Gilligan DM, Mohandas N, Peters LL (2008). Targeted deletion of alpha-adducin results in absent beta- and gamma-adducin, compensated hemolytic anemia, and lethal hydrocephalus in mice. Blood 112, 4298–4307.
Salomao M, Zhang X, Yang Y, Lee S, Hartwig JH, Chasis JA, Mohandas N, An X (2008). Protein 4.1R-dependent multiprotein complex: new insights into the structural organization of the red blood cell membrane. Proc Natl Acad Sci USA 105, 8026–8031.
Schevzov G, Whittaker SP, Fath T, Lin JJ, Gunning PW (2011). Tropomyosin isoforms and reagents. Bioarchitecture 1, 135–164.
Shen BW, Josephs R, Steck TL (1986). Ultrastructure of the intact skeleton of the human erythrocyte membrane. J Cell Biol 102, 997–1006.

Skau CT, Neidt EM, Kovar DR (2009). Role of tropomyosin in formin-mediated contractile ring assembly in fission yeast. Mol Biol Cell 20, 2160–2173.
Stark BC, Sladewski TE, Pollard LW, Lord M (2010). Tropomyosin and myosin-II cellular levels promote actomyosin ring assembly in fission yeast. Mol Biol Cell 21, 989–1000.
Stehn JR, Haass NK, Bonello T, Desouza M, Kottyan G, Treutlein H, Zeng J, Nascimento PR, Sequeira VB, Butler TL, *et al.* (2013). A novel class of anticancer compounds targets the actin cytoskeleton in tumor cells. Cancer Res 73, 5169–5182.
Sung LA, Gao KM, Yee LJ, Temm-Grove CJ, Helfman DM, Lin JJ, Mehrpouryan M (2000). Tropomyosin isoform 5b is expressed in human erythrocytes: implications of tropomodulin-TM5 or tropomodulin-TM5b complexes in the protofilament and hexagonal organization of membrane skeletons. Blood 95, 1473–1480.
Sung LA, Lin JJ (1994). Erythrocyte tropomodulin binds to the N-terminus of hTM5, a tropomyosin isoform encoded by the gamma-tropomyosin gene. Biochem Biophys Res Commun 201, 627–634.
Tojkander S, Gateva G, Schevzov G, Hotulainen P, Naumanen P, Martin C, Gunning PW, Lappalainen P (2011). A molecular pathway for myosin II recruitment to stress fibers. Curr Biol 21, 539–550.
Vlahovich N, Kee AJ, Van der Poel C, Kettle E, Hernandez-Deviez D, Lucas C, Lynch GS, Parton RG, Gunning PW, Hardeman EC (2009). Cytoskeletal tropomyosin Tm5NM1 is required for normal excitation-contraction coupling in skeletal muscle. Mol Biol Cell 20, 400–409.
Weber A, Pennise CR, Babcock GG, Fowler VM (1994). Tropomodulin caps the pointed ends of actin filaments. J Cell Biol 127, 1627–1635.
Yamashiro S, Gokhin DS, Sui Z, Bergeron SE, Rubenstein PA, Fowler VM (2014). Differential actin-regulatory activities of Tropomodulin1 and Tropomodulin3 with diverse tropomyosin and actin isoforms. J Biol Chem 289, 11616–11629.
Yoshida H, Kawane K, Koike M, Mori Y, Uchiyama Y, Nagata S (2005). Phosphatidylserine-dependent engulfment by macrophages of nuclei from erythroid precursor cells. Nature 437, 754–758.